Open Access Journal
Journal of Power Technologies 92 (3) (2012) 166–173
journal homepage:papers.itc.pw.edu.pl

Development and verification of work hardening models for X2CrNiMoN25-7-4 super duplex stainless steel after sigma phase precipitation hardening used for FEM simulations

Paweł Szabracki*, Mirosław Bramowicz, Tomasz Lipiński

University of Warmia and Mazury in Olsztyn, Faculty of Technical Sciences, Chair of Material and Machinery Technology, M. Oczapowskiego 2, Olsztyn, 10-719, Poland

Abstract

The aim of this study was to develop numerical work hardening models for super duplex stainless steel X2CrNiMoN25-7-4. Each model accounts for changes caused by the precipitation of a known quantity (0, 20, 35, 38%) of FeCr intermetallic phase (σ). The developed models were applied in FEM simulations of tensile tests for various geometries containing the same quantity of the sigma phase. Calculations were performed for two different geometries—flat and round tensile samples. Correlations between experimental and numerically simulated tensile curves were determined using Pearson's correlation coefficient. The obtained results revealed significant correlations (above 0.9955) between numerical and experimental data.

Keywords: Sigma phase, hardening, super duplex, FEM simulation, tensile test

1. Introduction

The application of temperatures higher than 320–330°C to stainless steel causes aging in this group of engineering materials. For this reason, stainless steel should be used at temperatures below 300–320°C. In some situations (failures, accidents), the operating temperature rises above the planned levels. The proposed work hardening models for X2CrNiMoN25-7-4 super duplex stainless steel account for structural variations resulting from changes in the sigma phase content after an accident. Following an accident, the temperature of structural elements increases to the temperature of sigma phase formation (600–800°C). Undesirable phases (sigma σ, delta ferrite δ and other) are formed at different rates in stainless steel. In many structures, the mechanical properties resulting from changes in microstructure have to be analyzed for safety reasons. Hardening after the precipitation of a Cr-rich sigma phase in stainless steel and non-metallic inclusions of carbon steel is an example of a heat-induced modification of mechanical properties. Sigma phase may precipitate in high quantities, and it significantly affects mechanical properties [1–3].

Laboratory control of the crystallization process supports observations of alloy microstructure (for example, the proportion of ferrite/austenite) [4]. Recrystallization cannot be controlled during production or operation. For this reason, analyses of microstructure may be required during operation or af-

*Corresponding author
Email addresses: pawel.szabracki@uwm.edu.pl (Paweł Szabracki*), miroslaw.bramowicz@uwm.edu.pl (Mirosław Bramowicz), tomasz.lipinski@uwm.edu.pl (Tomasz Lipiński)

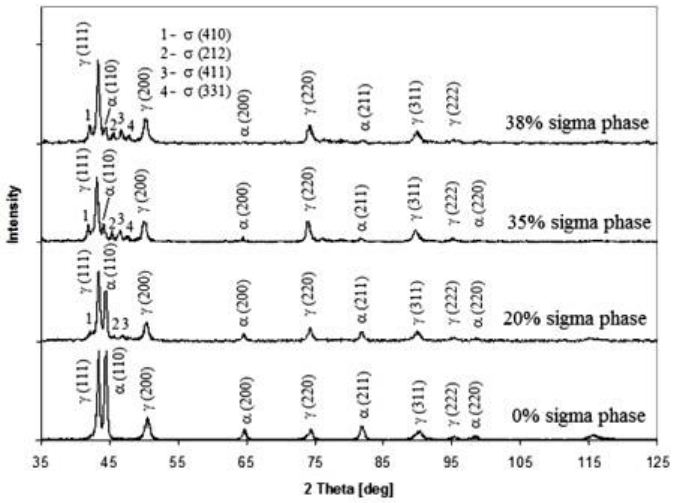

Figure 1: Diffraction patterns for X2CrNiMoN25-7-4 super duplex stainless steel with different sigma phase content

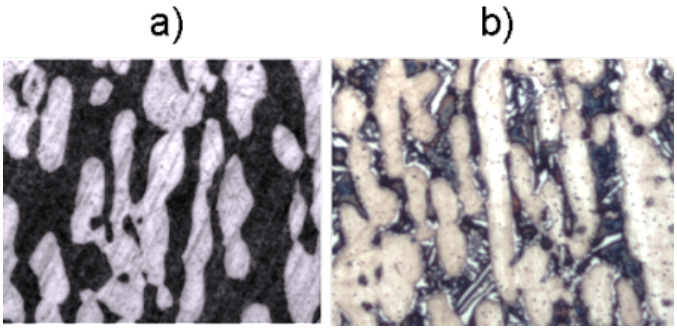

Figure 2: Micrographs of X2CrNiMoN25-7-4 super duplex stainless steel with a) duplex microstructure and b) 20% of the sigma phase in microstructure. Beraha reagent. Magn. 500x

ter accident/failure.

The existing structures with microstructural changes can be analyzed by FEM methods (Code_Aster Solver). Numerical models which describe work hardening of the material and account for microstructural changes have to be developed and verified for analysis of specific geometries (real structures). This paper describes the methodology for developing and applying work hardening models in elasto-plastic nonlinear FEM simulations.

Statistical data (component temperature) obtained during continuous measurements can be used to predict microstructural changes in construction elements made of X2CrNiMoN25-7-4 [5]. Microstructural changes modify the mechanical properties of material. Changes in mechanical behavior which correspond to microstructural alterations support analyses of pressure component safety after accidents.

2. Methodology

2.1. Microstructure analysis

In duplex stainless steel, sigma phase can result from the direct transformation of ferrite (α) in the aging process or the eutectoid transformation of ferrite (δ) into secondary austenite (γ_2) and sigma phase (σ) [2, 3]. Phase fractions in X2CrNiMoN25-7-4 stainless steel were determined using X-ray Diffraction (XRD) and magnetic induction methods. Diffraction measurements were performed on a XPERT PRO diffractometer with CuK_α radiation. X-ray diffraction patterns for X2CrNiMoN25-7-4 samples with various sigma phase content are shown in Fig. 1. Profile lines of XRD reflexes were described using the Cauchy function and a self-designed application [6].

Austenite (γ) and sigma phase (σ) are non-magnetic phases. Magnetic induction supports fast and non-invasive determinations of ferrite content (decrease from initial value) in the existing structure. FERITSCOPE MP30 with an EGABW1.3-Fe probe was used for a quick determination of ferrite content in the analyzed super duplex stainless steel. XRD methods are more time consuming and, in most cases, they require sample collection or interference with the existing object. Phase fractions in X2CrNiMoN25-7-4 steel for different heat treatment parameters are shown in Table 1.

Metallographic micrographs were acquired using the OLYMPUS IX70M microscope, and phase fractions were determined with the application of ImageJ software. An example of a duplex microstructure (ferrite α—45%, austenite γ—55%) after chemical etching (Beraha reagent) is shown in Fig. 2a. Bright fields represent austenite grains and dark fields are indicative of ferrite grains. An example of a duplex microstructure with 20% of the sigma phase is presented in Fig. 2b. The presence of sigma phase σ (20%) was noted in this microstructure, which also contained ferrite α (30%) and austenite γ (50%). Sigma phase grains were represented by white fields.

Table 1: Phase fractions in X2CrNiMoN25-7-4 super duplex stainless steel after solutioning (row 1) and aging (rows 2–4)

No.	Phase fraction [%] Metallographic			XRD			Magnetic	Heat treatment parameters		
	γ	α	σ	γ	α	σ	α	Temperature, °C	Time, min	Cooling
1	55	45	-	55	45	-	45	1100	30	water
2	50	32	18	50	30	20	25	800	30	water
3	54	12	34	55	10	35	7	800	60	water
4	55	7	38	56	6	38	2	800	120	water

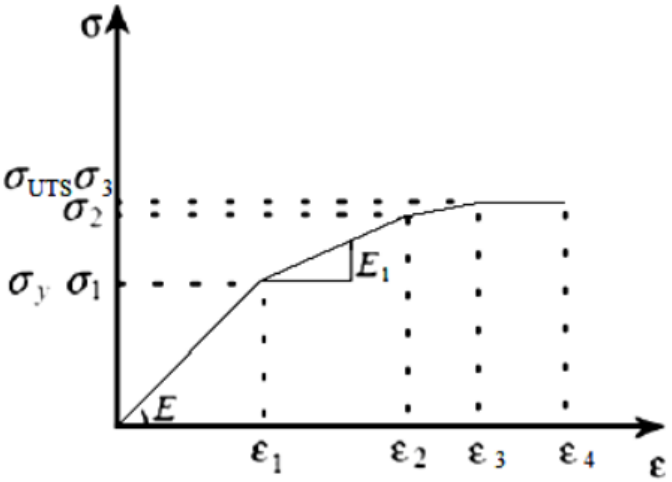

Figure 3: Work hardening in Code_Aster solver [7]

Detailed results of metallographic measurements are summarized in Table 1.

2.2. *Preparing models of work hardening after sigma phase precipitation*

Changes in the strength parameters of X2CrNiMoN25-7-4 stainless steel caused by aging were determined experimentally based on results of the tensile test and in accordance with standard PN EN ISO 6892-1 for different sigma phase contents (20, 35, 38%) [8]. The obtained results and limits for solver Code_Aster (EDF R&D—solver used for FEM calculations) were used to determine tensile curves for the initial duplex microstructure and different sigma phase contents (20, 35, 38%) in X2CrNiMoN25-7-4 stainless steel. This section of the paper outlines the procedure of developing numerical work hardening models for X2CrNiMoN25-7-4 super duplex stainless steel [9–13]. The use of Code_Aster solver in simulations accounted for material work hardening according to formula 1 (Fig. 3).

$$R(p) = \sigma(i) + \frac{\sigma_{i+1} - \sigma_i}{p_{i+1} - p_i}(p - p_i) \tag{1}$$

$$p_i = \varepsilon_i - \frac{\sigma_i}{E} \tag{2}$$

The developed models were subjected to nominal stress, MPa, and strains. The first point in the numerical model of hardening (traction data) should be equal to material yield strength (YS). Code_Aster uses the first point on the curve to calculate Young's modulus according to formula 3. In this case, yield strength and Young's Modulus are material properties, and ε_{YS} has to be calculated (3) for the correct interpretation of material properties.

$$E = \frac{\sigma_{YS}}{\varepsilon} \tag{3}$$

The last point in the developed numerical model is equal to ultimate tensile strength (UTS). The subsequent linear parts of the curve should have a decreasing slope (4). When the material attains UTS value, stress ceases to increase and remains constant. The first UTS values reached in specific areas indicate locations with highest probability of damage.

$$E_i > E_{i+1} \tag{4}$$

Work hardening models for X2CrNiMoN25-7-4 steel after sigma phase precipitation (20, 35, 38%) are shown in Fig. 4. The characteristic points (YS, UTS) for each sigma phase fraction in the microstructure are presented in Table 2.

Table 2: Characteristic points for X2CrNiMoN25-7-4 super duplex stainless steel after solutioning (row 1) and aging (rows 2–4)

No.	Yield Strength (YS), MPa	Ultimate Tensile Strength (UTS), MPa	Heat treatment parameters Temperature, °C	Time, min	Cooling
1	621	862	1100	30	water
2	747	952	800	30	water
3	825	1024	800	60	water
4	832	985	800	120	water

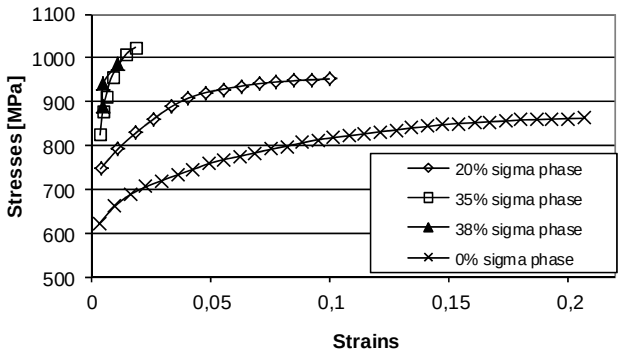

Figure 4: Work hardening models for different sigma phase fractions in X2CrNiMoN25-7-4 super duplex stainless steel

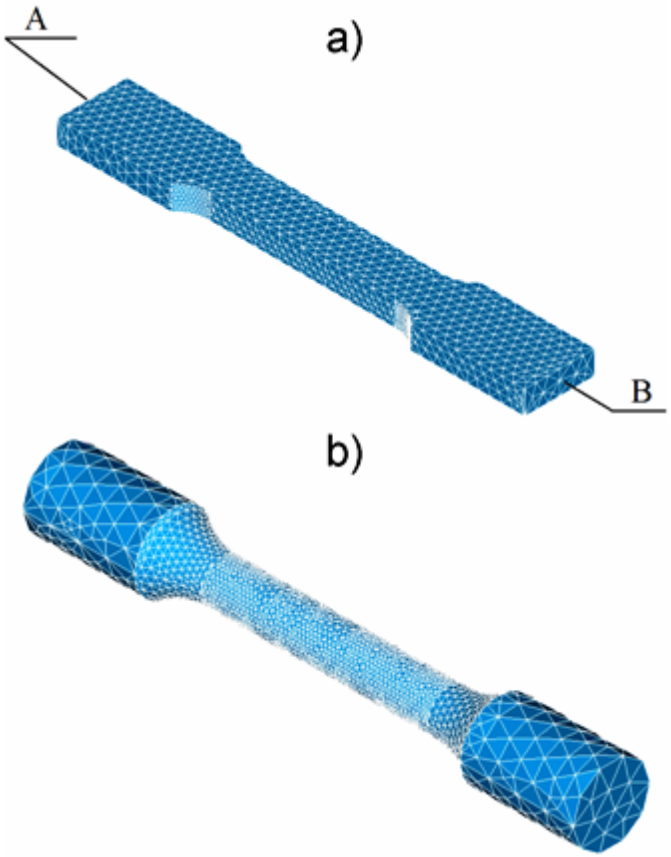

Figure 5: Meshes used for tensile test simulation. Flat sample a) and round sample b)

2.3. *Meshing, defining tensile test boundary conditions and verification*

The developed work hardening models for X2CrNiMoN25-7-4 stainless steel were used to simulate tensile tests of flat a) and round b) samples (Fig. 5).

A flat mesh contained 1900 nodes, 2662 surface elements (triangles) and 6 891 volume elements (tetrahedrons). A round mesh comprised 4 458 nodes, 6 032 surface elements (triangles) and 16 544 volume elements (tetrahedrons). The meshes were developed using the French Open Source Integration Platform for Numerical Simulations (SALOME v6).

During the test, one surface of each sample (surface B in Fig. 5a) was locked (displacement dx=dy=dz=0), whereas the opposite surface (surface A in Fig. 5a) was moving along the specimen. Stress and strain distributions in the studied samples were calculated for different time steps (displacement of surface A in time).

The displacement of surface A (Fig. 5a) was constant in time and equal to Δl=0.5 mm/sec. Differences were noted in displacement increment Δl (Fig. 6) for calculation steps in various sections of the stress-strain curve. The length of the initial sample was l_0=100 mm. Values of the displacement increment applied in calculations for different ranges of sample length l_i (Fig. 6) are shown in Table 3. Stress-strain curves, the product of numerical simulations, were determined at the center of symmetry in flat and round samples.

Correlation methods are often used to compare the

Table 3: Displacement increment for different ranges of flat sample length li (Fig. 6) and different sigma phase fractions

Sigma phase fraction, %	Elastic deformation range, mm		Initial part of plastic deformation, mm		Final part of plastic deformation, mm	
	Range	Step Δl	Range	Step Δl	Range	Step Δl
0	100–101	0.1	101–106	0.5	>105	1
20	100–101	0.1	>101	0.5	-	-
35	100–101	0.1	>101	0.5	-	-
38	100–101	0.1	>101	0.5	-	-

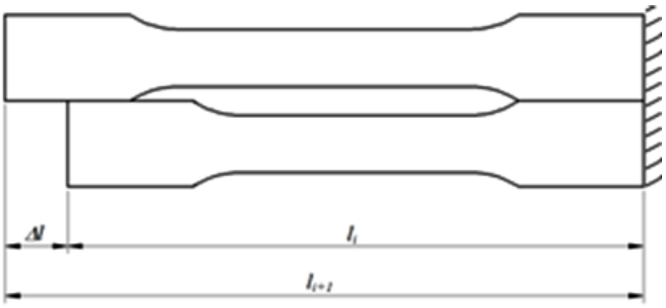

Figure 6: Displacement increment during calculations

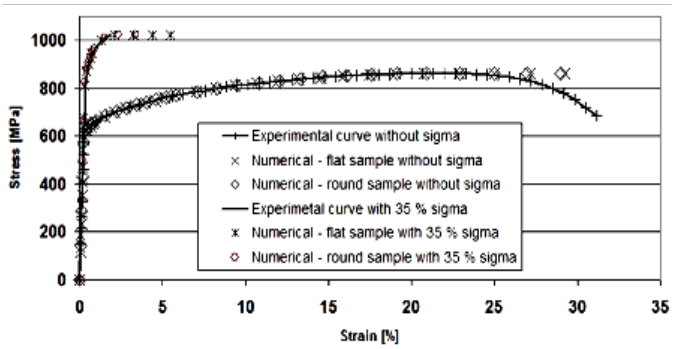

Figure 9: Experimental and numerical tensile curves for initial duplex microstructure and containing 35% of sigma phase

results of numerical simulations with experimental data [14]. To compare experimental stress-strains curves with the results of numerical calculations, Pearson's correlation coefficient (5) was used in the 0-UTS stress range (numerical models do not describe neck formation) for each sample [15, 16].

$$r_{xy} = \frac{cov\,(xy)}{\sigma_x \sigma_y} \tag{5}$$

$$\sigma_x = \sqrt{\frac{\sum_{i=1}^{n} (x_i - \overline{x})^2}{n}} \tag{6}$$

$$\sigma_y = \sqrt{\frac{\sum_{i=1}^{n} (y_i - \overline{y})^2}{n}} \tag{7}$$

3. Results

Stress distribution in a deformed flat sample (at UTS value) with different sigma phase fractions is shown in Fig. 7. The highest plastic deformation (for UTS) was reported in duplex microstructures (Fig. 4, Fig. 7a). Sample elongation decreased with an increase in sigma phase fraction (Fig. 4, Fig. 7 b–d). The elongation of samples with duplex microstructure (to reach UTS value in the working part of the sample) was equal to Δl=15 mm. When sigma phase accounted for 20% of microstructure, UTS values were achieved at elongation of Δl=6.5 mm. The required elongation to reach UTS value was Δl=1.5 mm in microstructure with 35% sigma phase content and Δl=1 mm in microstructures with 38% sigma phase content. The initial ductile duplex microstructure becomes brittle when sigma phase fraction is higher than 35%. An intermediate state is achieved between ductile and brittle microstructure when sigma phase content reaches 20%. Blue areas in the sample (0 MPa) represent initial geometry before the tensile test.

Stress distribution in a deformed round sample (at UTS value) with different sigma phase fractions are shown in Fig. 8. The length increment required to attain UTS value was identical to that noted in flat samples (it decreased with an decrease in the ferrite (α) content of microstructure).

Numerical results for flat and round samples were imposed on experimental curves to compare calcu-

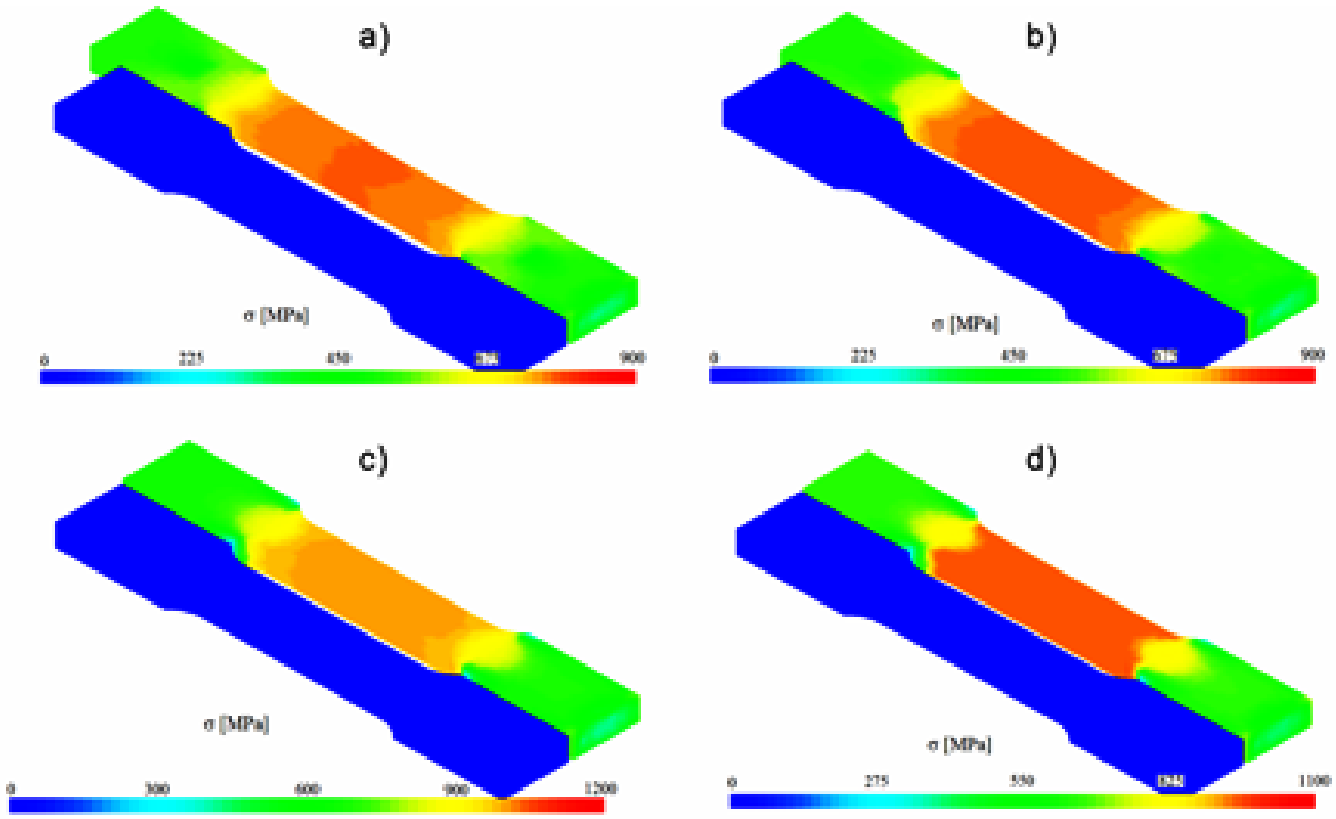

Figure 7: Stress distributions in deformed flat sample (UTS reached) with different sigma phase fraction: a) 0%, b) 20%, c) 35% and d) 38% of the sigma phase

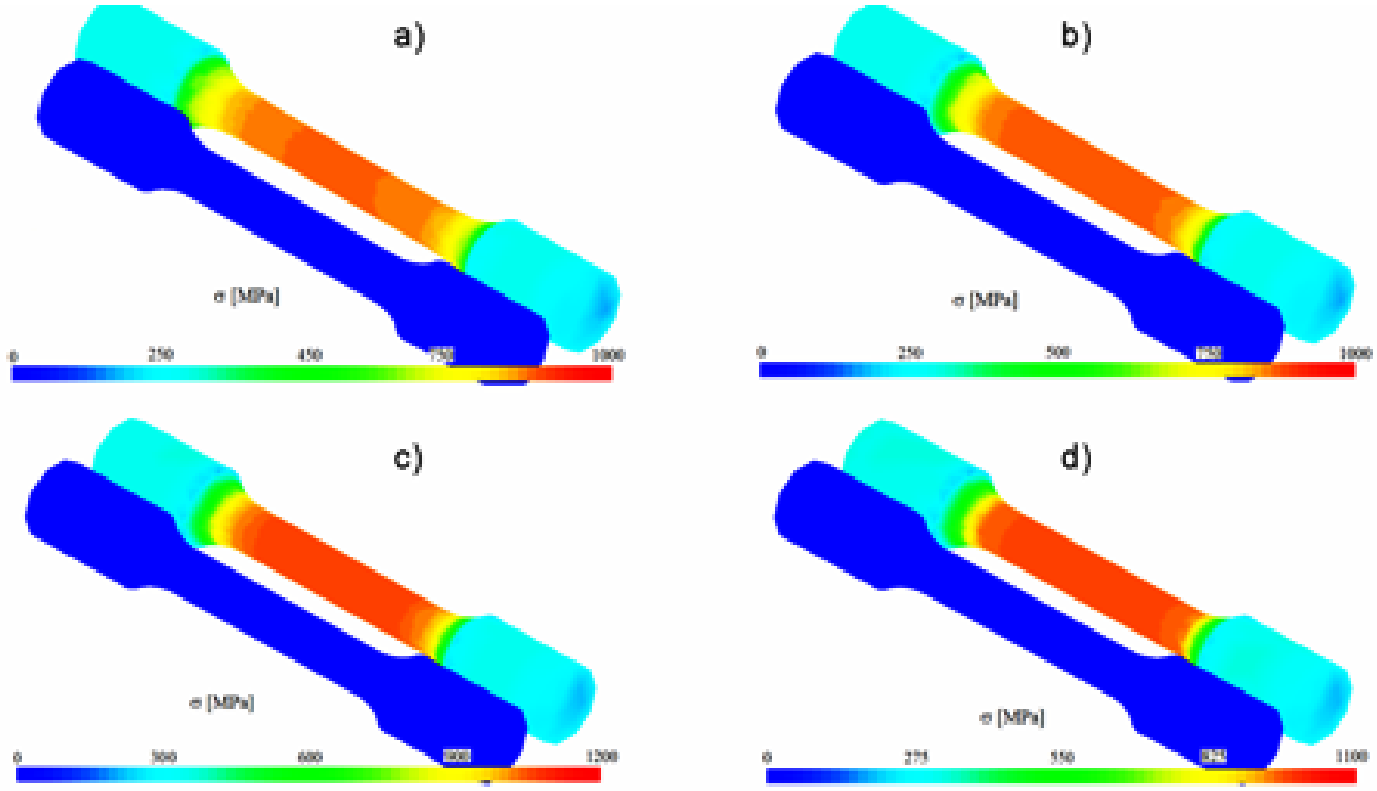

Figure 8: Stress distributions in deformed round sample (UTS reached) with different sigma phase fraction: a) 0%, b) 20%, c) 35% and d) 38% of the sigma phase

Table 4: Pearson correlation coefficient for flat and round tensile sample

Sigma phase fraction, %	Pearson's correlation coefficient for flat sample	Pearson's correlation coefficient for round sample
0	0.9974	0.9989
20	0.9963	0.9956
35	0.9961	0.9966
38	0.9965	0.9966

lation results with experimental data. Numerical stress-strain curves determined for the center of symmetry were used in both cases. This point was chosen due to the symmetry of samples. Experimental stress-strain curves for 0 and 20% sigma phase content, calculated numerically for round and flat samples, are presented in Fig. 9. Pearson's correlation coefficient was determined for round and flat samples. The values of Pearson's coefficient calculated for both geometries and different sigma phase fractions are shown in Table 4. In all cases, the coefficient of correlation is higher than 0.9955.

4. Conclusions

Based on the obtained results, the developed work hardening numerical models of X2CrNiMoN25-7-4 super duplex stainless steel can be used in safety analyses of components with various sigma phase fraction. Under typical operating conditions of a LWR primary loop (temperature below 320°C), sigma phase precipitation is not induced in X2CrNiMoN25-7-4 super duplex stainless steel. The proposed models can be applied in tests which analyze the strength behavior of X2CrNiMoN25-7-4 steel components after accidents that involve an increase in temperature. High temperature (600–800°C) induces sigma phase precipitation in duplex stainless steel.

In some structures, microstructural changes induced by an accident and their effect on the mechanical properties of the studied material cannot be an-

alyzed. The proposed methodology supports the development of numerical models describing changes in the mechanical properties of the analyzed material that follow from microstructural alterations. Such models should be developed for specific materials and manufacturing processes involved in the production of various components. Heat treatment parameters should be selected in view of their influence on the mechanical properties of the analyzed material.

References

[1] T. Lipiński, A. Wach, Analysis of the dimensional structure of non-metallic inclusions in high-grade medium carbon steel, Archives of Metallurgy and Materials 57 (2).

[2] J. Nowacki, Stal duplex i jej spawalność, WNT, 2009.

[3] S. Topolska, J. Łabanowski, Effect of microstructure on impact toughness of duplex and superduplex stainless steels, Journal of Achievements in Material and Manufacturing Engineering 36 (2009) 142–149.

[4] W. Wołczyński, T. Okane, J. Kloch, R. Ebner, Formation of the doublets during oriented growth of the fe-4.34ni alloy, Archives of Metallurgy 46 (2001) 293.

[5] K. Świrski, Power plant performance monitoring using statistical methodology approach, Journal of Power Technologies 91 (2) (2011) 63–76.

[6] P. Szabracki, M. Bramowicz, T. Lipiński, The computer analysis shape of reflexes xrd on the basis of x2crnimon25-7-4 steel, Technical Sciences 13 (2010) 266–281.

[7] Code Aster document R5.03.02.

[8] PN-EN ISO 6892-1:2010 - Metale. Próba rozciągania. Część 1: Metoda badania w temperaturze otoczenia.

[9] Code Aster document U4.43.01.

[10] Methodes d'analyse mecanique pour le traitment d'écarts, EDF SEPTEN internal document.

[11] F. Rossillon, Y. Meziere, Analysis of fracture specimen failure of inconel 600: elastic-plastic calculations and thermo plastic energy fracture parameter, in: PVP2010-25323, 2010.

[12] P. Szabracki, Fracture behavior of nickel based alloy 600 of ductile tearing, Tech. rep., EDF SEPTEN internal report.

[13] [link].
URL `www.edf.com`

[14] Y. Lahssuny, W. Jędral, Universal correlations for predicting complete pump performance characteristics, Journal of Power Technologies 89/90.

[15] W. Ignatczyk, M. Chromińska, Statystyka teoria i zastosowanie, Wydawnictwo Wyższej Szkoły Bankowej, Poznań, 1999.

[16] J. Taylor, Wstęp do analizy błędu pomiarowego, Państwowe Wydawnictwa Naukowe, Warszawa, 1999.